The role of surface microstructures in particle-droplet coalescence and jumping from superhydrophobic surfaces

Surfaces and Interfaces 64 (2025) 106333

Contents lists available at ScienceDirect

Surfaces and Interfaces

journal homepage: www.sciencedirect.com/journal/surfaces-and-interfaces

The role of surface microstructures in particle-droplet coalescence and jumping from superhydrophobic surfaces

Konstantinos Konstantinidis [a], Johan Göhl [b], Andreas Mark [b,a], Xiao Yan [c,d,e], Nenad Miljkovic [e,f,g,h,i], Srdjan Sasic [a,*]

[a] Division of Fluid Dynamics, Department of Mechanics and Maritime Sciences, Chalmers University of Technology, Gothenburg, SE 412 96, Sweden
[b] Fraunhofer–Chalmers Center, Chalmers Science Park, Gothenburg, SE 412 88, Sweden
[c] Key Laboratory of Low-grade Energy Utilization Technologies and Systems, Chongqing University, Ministry of Education, Chongqing, 400030, China
[d] Institute of Engineering Thermophysics, Chongqing University, Chongqing, 400030, China
[e] Department of Mechanical Science and Engineering, University of Illinois, Urbana, IL 61801, United States
[f] Department of Electrical and Computer Engineering, University of Illinois, Urbana, IL 61801, United States
[g] Materials Research Laboratory, University of Illinois, Urbana, IL 61801, United States
[h] Institute for Sustainability, Energy and Environment (iSEE), University of Illinois, Urbana, IL, United States
[i] International Institute for Carbon Neutral Energy Research (WPI-I2CNER), Kyushu University, 744 Moto-oka Nishi-ku, Fukuoka 819-0395, Japan

ARTICLE INFO

Keywords:
Microstructured superhydrophobic surfaces
Droplet spreading on a particle
Self-cleaning
Particle-droplet jumping
VOF-immersed boundary
Dynamic contact angle

ABSTRACT

We study here by direct numerical simulations how geometrical and wetting properties of rectangular pillar-shaped microstructured superhydrophobic surfaces affect the process of particle-droplet coalescence and jumping. Such a process represents a passive mechanism of self cleaning where a single droplet coalesces with a particle of micrometer size, spreads on the particle and drives particle-droplet jumping. An in-house volume of fluid-immersed boundary framework is used to study the influence of characteristic dimensions of pillars (width, solid area fraction and height) and contact angles on particle-droplet coalescence and jumping. We relate our results for pillared surfaces to those obtained when using corresponding planar superhydrophobic surfaces. A range of different behaviors are disclosed when it comes to energy dissipation mechanisms and outcome of the coalescence and jumping process for these two types of superhydrophobic surfaces. We quantify and explain how the detachment of the particle-droplet system from a pillared substrate takes place at a later stage than that from a corresponding planar substrate. A reduced effect is demonstrated on the process of having configurations with a larger distance between the pillars and that longer pillars facilitate earlier jumping as compared to that on surfaces with shorter pillars. We also look at the transition between Cassie-Baxter and Wenzel states (determining whether jumping of the particle-droplet system will take place at all) as a function of wetting properties of the surfaces. Our results contribute to optimization of superhydrophobic surfaces aiming to achieve an enhanced self-cleaning efficiency.

1. Introduction

Superhydrophobic surfaces have found numerous industrial applications featuring water-repellent [1], self-cleaning [2,3], anti-icing [4,5], anti-corrosion [5], defrosting [6] and enhanced heat-transfer properties [7,8]. Inspired by natural surfaces found in lotus leaves, mosquitoes and cicadas, these surfaces promote high-contact angles with water-based liquids [9–13]. One method to achieve superhydrophobicity in the mentioned applications involves the use of strategically placed micron-sized pillar-shaped vertical structures or protrusions [1,12,14]. They take advantage of the innate hydrophobicity of the outer surface layer of a substrate to attain to the surface superhydrophobic properties. Typically, superhydrophobic surfaces exhibit low surface energy [15] and low work of adhesion [16], which is the energy required to separate a liquid from a solid surface. These properties, often provided by the chemical composition of a surface, potentially induce a number of mechanisms for removal of droplets from the surfaces. However, microstructured surfaces do not necessarily possess low surface energy [16], leading to a wide range of behaviors present in different applications.

Previous research has established links between roughness (and textured patterns in general, such as those with pillars) and the high apparent contact angles of superhydrophobic surfaces [17]. Cassie-Baxter

* Corresponding author.
E-mail address: srdjan@chalmers.se (S. Sasic).

https://doi.org/10.1016/j.surfin.2025.106333
Received 9 December 2024; Received in revised form 7 March 2025; Accepted 26 March 2025
Available online 5 April 2025

wetting theory explains how air pockets trapped between a droplet and surface roughness structures influence droplet interaction with the substrate, create liquid bridges and enhance contact angles [18,19]. In this respect, the droplet-to-pillar size ratios are of great relevance for determining the overall dynamics of the wetting process. While pillars tend to enhance the apparent contact angles and the Laplace pressure inside a droplet, dynamic situations cause pinning formations during droplet movement [20]. Studies have shown that nano-scale roughness, with hair-like structures of up to 500 nm, can reduce pinning and limit the sliding angle and the contact angle hysteresis for the surface in question [21].

A notable feature of superhydrophobic surfaces is that they enable a specific scenario of self-removal of droplets, known as the jumping droplets phenomenon [22,23]. There, two droplets coalesce on a superhydrophobic surface, involving the following sequence of events that lead to an eventual jumping of the merged droplet: interaction of the liquid bridge between the droplets with the superhydrophobic substrate, a series of the merged droplet shape oscillations and, finally, its departure from the surface. The process is driven by the interaction of capillary and inertial forces after the release of the surface energy during coalescence, accompanied by a low viscous dissipation [23,24]. Numerous studies looked at, among other things, the jumping velocity and efficiency of the process [25–27], as well as the influence of surface modifications such as ridges and pillars [7,28–30]. However, the jumping droplets phenomenon as a mechanism for removal of droplets from structured superhydrophobic surfaces can be of low efficiency at certain scales and configurations [28,31].

Self-cleaning on superhydrophobic surfaces can occur both with and without microstructures present [21,28,32]. Having a microstructured surface, however, facilitates decreasing the contact angle in order to achieve similar wetting behaviors, while reducing the need for applying complex surface treatments such as nanocoatings and similar [33,34]. The droplets residing on structured surfaces exhibit strong capillary and surface tension forces since they are typically smaller than the capillary length and they thus belong to a more general capillary-inertial dominated transport mode [22]. In several studies that dealt with self-cleaning benefiting from the jumping droplets process, a relatively small influence of microstructures was found [35]. Different conclusions were, however, drawn for the cases where the characteristic microstructure dimensions (typically, the size of the pillars) become comparable to the involved droplet sizes [28]. The question of the influence of the type of surface becomes even more interesting when we look at the removal of contaminants (i.e. particles) from superhydrophobic surfaces by a single droplet. Yan et al. [36] were the first to show experimentally that a droplet, settled on a homogeneous superhydrophobic substrate with very high apparent contact angles and a low degree of hysteresis, spontaneously initiates spreading to a spherical hydrophilic particle. This leads to droplet shape oscillations, caused by the expansion of the contact area with the particle, while the body mass of the droplet approaches the particle. When the droplet expands on the superhydrophobic surface, this droplet-surface interaction initiates an upwards motion for the particle-droplet agglomerate (system). After jumping, the system keeps oscillating around the ideal contact area, and in the same time it rotates around its common center of gravity. Konstantinidis et al. [37] performed a numerical study to investigate the behavior of a particle-droplet system on a planar superhydrophobic surface. The authors suggested a representation for the capillary force acting on the particle and revealed a range of scenarios related to different energy dissipation mechanisms as a function of the droplet-to-particle size ratio, wettability of the particle and the surface contact angles and contact-angle hysteresis. In this work we will analyze, explain and quantify the effect of having a microstructured surface on the particle-droplet coalescence and jumping process.

Studies involving different patterned (or microstructured) surfaces often focus on identifying and obtaining maximum contact angles [33,35], but also look at droplet pinning phenomena that are of great relevance in dynamic situations [38]. Pinning is, for example, observed during the movement or shedding of the droplet on top of pillared structures [39]. Sun et al. [16] increased and afterwards reduced the volume of droplets on top of structured surfaces to measure the adhesive and repelling forces, and then compared them with simplified analytical estimations. The authors pointed out that the dynamic behavior of such forces differs from that of the capillary forces during a shedding motion of a droplet. Yeong et al. [40] also studied the contact line behavior during vertical movement of droplets and highlighted the differences in the pinning force between that case and the one when shedding movement is present. The same study demonstrated that the receding forces peak in the middle of the top region of the pillar and that at the same location the dynamic receding contact angle obtains its lowest value.

The interaction of droplets with structured surfaces has also been studied numerically. In general, numerical studies have introduced pillars in rectangular or cylindrical forms. Attarzadeh and Dolatabadi [28] simulated the droplet coalescence and jumping from a structured surface. The authors used the microscopic intrinsic contact angle of the surface for the contact-angle implementation on the pillars. In the same study a dynamic contact-angle model was implemented to estimate the contact-angle hysteresis present on the surfaces of the pillars, effectively modeling the pinning phenomenon. We note that introducing a moving hydrophilic particle in such a system, where a droplet is simultaneously spreading on both the particle and on top of the pillars dramatically increases the complexity of such simulations. We are at the moment not aware of any numerical study that looks at the complex dynamical behavior and the dissipative influence of a structured surface on the process of particle-droplet coalescence and jumping.

In this work we thus present direct numerical simulations of all stages of particle-droplet coalescence and jumping from a microstructured surface. We provide a comprehensive analysis on how geometrical and wetting properties of rectangular pillared surfaces define various scenarios and outcomes of the process. In particular, we look at the influence on the overall jumping efficiency of the width and height of the pillars, their relative placement and the wetting properties. We also examine qualitatively and quantitatively the wetting area of the substrate through a series of advancing and retracting motions of the contact line on top of the pillars. Finally, we quantify the energy losses when varying the mentioned parameters. It is to be noted that, to the best of our knowledge, the present work is the first multiphase DNS study that aims at revealing fundamental features of this complex interaction between a coalescing and jumping particle-droplet system and a pillared supehydrophobic surface. Our task is not made easier having in mind the absence of corresponding experimental studies. Numerous challenges exist when attempting to study numerically the synergetic effect of the presence of complex interfaces, movement of the three-phase contact line, wetting of a (highly) curved boundary (such as that of the particle surface), and interaction of the particle-droplet system with complex geometrical structures (pillars). Open research questions comprise the lack of knowledge related to the adhesion physics, particularly in dynamic spreading during the liquid bridge formation and the limited (and insufficiently validated) models formulated to describe capillarity adhesion in Eulerian frameworks. By accounting for the mentioned phenomena in a rigorous manner within a comprehensive multiphase DNS framework, our work provides guidelines for designing superhydrophobic surfaces that facilitate the type of the self-cleaning process treated in this study.

The remainder of the paper is structured as follows: in Section 2 we present the comprehensive volume of fluid-immersed boundary numerical framework used in the present work. Then, we go into the configuration of the simulation cases and illustrate geometrical and wetting properties of the different substrates used. Following, in Section 4, we present the results of our study followed by a discussion and analysis of the observed outcomes. Lastly, in Section 5 we summarize our main findings.

2. Methods and configuration

2.1. Methods

In this study we use the in-house software IPS IBOFlow to compute the droplet hydrodynamics and its spreading on the particle, interaction of the particle-droplet system with the microstructured surface and to calculate the forces acting on the particle and its resulting motion. The software comprises the volume-of-fluid (VOF) and the immersed boundary methods (IBM) to capture the sharp interface movements and to take into account the conditions at the solid surfaces of the substrate and the particle. The use of IBM in our work is essential for capturing the dynamics of a moving particle, as well as for the inclusion of pillars and proper implementation of the boundary conditions on their surface. With the developed framework, the computational mesh does not need to adjust to any new locations of the particle, as well as that it can accommodate the existence of pillars under a grid resolution reduced to that required if a boundary-adjacent mesh were used. The continuum surface force approach (CSF) [41] is used for the surface tension force, while the curvature of the interface is represented by the gradient of the volume fraction field.

While detailed descriptions of the numerical framework were provided in our previous work [37], we highlight here that the framework uses the mirrored immersed boundary method [42,43], a dynamic contact angle model by Kistler [44] for both advancing and receding contact line movements, and a Navier slip boundary condition to remove the moving contact line stress singularity problem [27,45]. Additionally, the continuum capillary force (CCF) [46,47] is used on the moving particle as adopted in Konstantinidis et al. [37]. The most important parts of the framework are given below.

The two-phase flow is represented by a single–fluid approach, solved for the velocity $\boldsymbol{v}$ and pressure p fields:

$$\nabla \cdot \boldsymbol{v} = 0\,,$$
$$\frac{\partial(\rho \boldsymbol{v})}{\partial t} + \boldsymbol{v}\cdot\nabla(\rho \boldsymbol{v}) = -\nabla p + \nabla\cdot(\mu\nabla \boldsymbol{v}) + \rho\,\boldsymbol{g} + \mathbf{f}_{\mathrm{SF}}\,. \tag{1}$$

The density ρ and dynamic viscosity μ depend on the interface location, $\boldsymbol{g}$ stands for the gravitational acceleration and $\mathbf{f}_{SF}$ is the normal surface tension force per unit volume acting at the interface. In VOF the interface advection is given by:

$$\frac{\partial \alpha}{\partial t} + \boldsymbol{v}\cdot\nabla\alpha = 0\,, \tag{2}$$

where α is the volume fraction.

The surface tension body force $\mathbf{f}_{SF}$, as mentioned, is given by the continuum surface force (CSF) model:

$$\mathbf{f}_{\mathrm{SF}} = \sigma\kappa\boldsymbol{n}\,, \tag{3}$$

where σ is the surface tension at the interface, κ is the curvature and $\boldsymbol{n}$ the interface normal vector at the interface.

The curvature κ of the interface is given by $\kappa = -\nabla\cdot\hat{\boldsymbol{n}}$, with the unit normal vector $\hat{\boldsymbol{n}}$ obtained from:

$$\hat{\boldsymbol{n}} = \frac{\boldsymbol{n}}{\|\boldsymbol{n}\|} = \frac{\nabla\alpha}{\|\nabla\alpha\|}\,. \tag{4}$$

The advancing and receding contact angles are given with the Kistler dynamic contact angle model, utilizing a modified Hoffman function [48]. The IBM equations provide the total hydrodynamic force $\mathbf{F}_{\mathrm{IB}}$ and torque $\mathbf{T}_{\mathrm{IB}}$ by computing the fluid stress $\boldsymbol{t}_{\mathrm{dS}}$ projected to the unit normal vector of the particle surface $\hat{\boldsymbol{n}}_{\mathrm{dS}}$:

$$\mathbf{F}_{\mathrm{IB}} = \int_{A_{\mathrm{tr}}} \boldsymbol{t}_{\mathrm{dS}}\cdot\hat{\boldsymbol{n}}_{\mathrm{dS}}\,dS \qquad \text{and} \tag{5}$$
$$\mathbf{T}_{\mathrm{IB}} = \int_{A_{\mathrm{tr}}} r\times(\boldsymbol{t}_{\mathrm{dS}}\cdot\hat{\boldsymbol{n}}_{\mathrm{dS}})\,dS\,. \tag{6}$$

The equation that gives the capillary force $\mathbf{F}_{cap}$ at the contact line C_l and that is tangential to the interface ($\hat{\boldsymbol{t}}_{int}$) is obtained from:

$$\mathbf{F}_{cap} = \int_{C_l} \sigma\,\hat{\boldsymbol{t}}_{int}\,dl\,. \tag{7}$$

Then, the CCF model returns a force per unit volume $\mathbf{f}_{CCF}$ for each cell according to:

$$\mathbf{f}_{CCF} = \sigma \boldsymbol{t}_{int}(\nabla\alpha\cdot\boldsymbol{t}_{C_l})(\nabla\chi\cdot\boldsymbol{n}_{dS}), \tag{8}$$

where χ is the solid fraction at the cells close to the solid surface. $\boldsymbol{t}_{C_l}$ is the interface outwards vector, a tangent to the solid surface. The total capillary force on the particle $\mathbf{F}_{CCF}$ is given by integrating for all the cells $\mathbf{F}_{CCF} = \sum_{V_i}\mathbf{f}_{CCF}\,\Delta V_i$, with V_i as the cell volume.

The analytical capillary force for a spherically-shaped droplet wetting a spherical particle is given by:

$$\mathbf{F}_{cap,ideal} = 2\pi\sigma R_p \sin a\cos\psi\,, \tag{9}$$

where R_p is the particle radius, a is the spreading angle on the particle and $\psi = f(\theta, a)$ is the angle between the local force at the interface and the total force to the particle, which is parallel to the direction of the centerline of the spheres. The angle ψ is a function of the contact angle on the particle and of the angle a.

When adapting the CCF model to the case of a droplet spreading over a spherical particle and the subsequent particle-droplet jumping, Konstantinidis et al. [37] proposed the capillary force as the average value between the analytical force $\mathbf{F}_{cap,ideal}$ and the computed CCF value $\mathbf{F}_{CCF}$. Such a representation was supported by a grid study for the balance of the capillary- and the hydrodynamic forces on the particle and validated by comparing with experimental data.

In Section 4 we will analyze the energy budget in different cases by normalizing the calculated values of different components of the droplet and particle-droplet kinetic energies with the total released surface energy of the system. To obtain the latter, we use the procedure described in detail in our previous work and the reader is advised to check those references [36,37].

Finally, the motion of the particle is a result of the fluid stresses acting on it, capillary and gravitational forces. The following equations provide the motion of the particle for each time step of the calculations:

$$m_{\mathrm{P}}\frac{d\boldsymbol{v}_{\mathrm{P}}}{dt} = \sum_{\mathrm{i}} F_{\mathrm{i}} = \mathbf{F}_{\mathrm{IB}} + \mathbf{F}_{\mathrm{CCF}} + \mathbf{F}_{\mathrm{gravity}}\,, \tag{10}$$

$$\mathbf{I}\frac{d\boldsymbol{\omega}_{\mathrm{P}}}{dt} = \sum_{\mathrm{i}} T_i - \boldsymbol{\omega}_P\times(\mathbf{I}\cdot\boldsymbol{\omega}_P)\,. \tag{11}$$

where $\boldsymbol{\omega}_{\mathrm{P}}$ is the rotational velocity of the particle and $\mathbf{I}$ is the moment of inertia.

2.2. Configuration of the simulation cases

The structured surface with square-shaped pillars is created by an automated process that has as inputs the width w, the pitch (or step) between pillars s and height h, placing the pillars in a rectangular grid arrangement. The solid area fraction $\Phi = w^2/(w+s)^2$ characterizes the contact area of the liquid that wets only the top of the pillars as a factor to the total equivalent spreading area if the substrate were flat. Rectangular pillars are chosen having in mind a dual goal of our work, namely to both reveal the fundamental physics of the particle-droplet coalescence and jumping on microstructured surfaces and, in the same time, to follow the guidelines obtained from manufacturing and experimental practices. Such pillar shapes are also present in theoretical [35,49,50] and numerical studies that looked into their effect on the energy dissipation of jumping droplets [28,51] or into droplets bouncing from superhydrophobic surfaces [52].

We present in Table 1 five geometrical configurations used for this study. Note that the case termed S6 in the table only changes the wetting properties of S1, with reducing the advanced and receding static contact angles by 15°. The benchmark substrate (S1) has $w = 14$

Table 1
Overview of geometrical and wetting properties of the substrates used.

Substrate	Width	Pitch	Height	Solid area fraction	Contact Angle	
S#	w [μm]	s [μm]	h [μm]	Φ [–]	θ_{adv} [°]	θ_{rec} [°]
S1	14	28	24	0.11	107.5	102.5
S2	14	16.5	24	0.21	107.5	102.5
S3	20	40	24	0.11	107.5	102.5
S4	20	31	24	0.15	107.5	102.5
S5	20	40	45	0.11	107.5	102.5
S6	14	28	24	0.11	92.5	87.5

μm, $s = 28$ μm, $\Phi = 0.11$ and $h = 8$ μm. The substrate S2 has a reduced pitch and therefore Φ increases to 0.21. In S3 we increase the width of pillars to $w = 20$ μm and adjust the pitch to retain the same Φ as S1. With the substrate S4 we want to observe the influence of the pitch size but with the larger width than that of S3, so s is reduced to approximately 30 μm, which is very close to the pitch length used for S1 (the slight difference is due to forced grid adjustments). With the substrate S5 we want to investigate the effect of increasing the height of the pillars as compared to that in the benchmark S1 surface.

The values for the setup and shown in the table are selected in accordance with guidelines from previous experimental [35] and numerical studies [28] on microstructured (or heterogeneous) surfaces, which suggested a superhydrophobic nature of substrates having pillars with width $w \simeq 10–30$, the solid area fraction between $\Phi \simeq 0.05–0.20$ and the contact angles between 100°–115°. The droplet-to-pitch size ratio (R_d/s) is suggested to be 3–10, which defines our pillar sizes to the range of 10–40 μm. This choice comes from the fact that we adopt the droplet size from the experimental study of Yan et al. [36], where the authors worked with the droplet radius $R_d = 120$ μm and the particle radius $R_p = 80$ μm (the particle density is $\rho_p = 7800$ kg/m^3). The minimum size limitation is motivated by our decision to cover a pillar in our numerical framework with the grid resolution of at least 3 cells per pillar length. Our minimum cell resolution is 40 times smaller than the droplet radius and represents the biggest contribution to the computational costs, with using advanced mesh refinement for the fluid cells. We acknowledge that the degree of our resolution of the shorter pillars could be further discussed, but it was governed by the trade off between the available computational resources and the accepted standards of doing multiphase DNS in such cases.

We have selected other parameters in accordance with our previous numerical study on planar superhydrophobic surfaces [37] and thus chosen the particle contact angle of 55°. The normalization factors for the contact area and the contact line length at the droplet–substrate interface are provided by the contact area that a droplet would have if it resided on a superhydrophobic surface wetting it fully at an angle of 170°. The domain size, as well as the way we carry out the analysis of the available energy in the system also follow our previous numerical work [37]. Finally, we present the velocity and time as normalized with the corresponding capillary-inertial velocity- and temporal scales. The velocity $\boldsymbol{v}$ is scaled by the capillary-inertial scaling $U_{CI} = \sqrt{\sigma R_d/\rho_l}$. The normalized simulation time τ is obtained by dividing t with the capillary-inertial time scale ($\tau = t/\tau_{CI}$), where τ_{CI} is defined as $\tau_{CI} = \sqrt{\rho_l/(\sigma R_d^3)}$.

3. Validation of the simulation framework

3.1. Jumping from a structured vs. planar surface

As mentioned previously, there exists no experimental study with which we could directly compare our results. We thus have two goals in this section: (*i*) to show that the chosen representations of a pillared substrate indeed (and at least) *qualitatively* behave like a superhydrophobic surface that facilitates particle-droplet coalescence and jumping, and (*ii*) to point out already here that there are differences to expect in the *quantitative* outcomes (energy-wise and in the moment of jumping) related to the particle-droplet system's behaviors between the pillared and planar superhydrophobic surfaces. We fulfill both goals by comparing our results with those experimentally obtained by Yan et al. [36]. It is reasonable to expect that, when a planar substrate is substituted by a structured one with rectangular micropillars and superhydrophobic (but smaller) apparent contact angles, the nature of the interaction between the solid and liquid phases will be different in the two cases. In the same time, we expect that with introducing appropriate intrinsic contact angles the behavior of the structured surface will be superhydrophobic. In the mentioned experimental study, Yan et al. [36] used a planar nanostructured surface of CuO nanoblades, whereas Konstantinidis et al. [37] used that study to successfully validate their numerical results by creating a simplified planar surface through implementing dynamic contact angles equivalent to an extreme superhydrophobic surface ($\theta_{eq} = 170°$ and hysteresis of 3°). We make a step further in this section and validate our simulations against experiments [36] using the selected settings for the benchmark configuration S1, presented in Section 2.2. We see in Fig. 1 that we are able to reproduce also with a structured surface all the phases of a particle-droplet coalescence and jumping process, provided that we use the same droplet and particle properties as in the previous study [37]. To be more specific, in Fig. 1 we compare the snapshots made at the corresponding instants for the simulation on a structured substrate with those obtained experimentally [36] and numerically on a planar surface [37]. By comparing the images, we observe that, firstly, the chosen pillared surface behaves like a hydrophobic surface that facilitates jumping of the particle-droplet system and, secondly, that there is a delay of the moment of jumping of the system from the pillared as compared to that from the planar surface. Furthermore, we notice that the variations of the droplet shape are accurately captured by both numerical investigations. The planar surface facilitates a higher degree of elevation of the particle-droplet system than does the pillared one. Therefore, this validation test confirms that both our goals are fulfilled: (*i*) that the particle-droplet system on a structured surface also goes through all the stages previously identified [37], and (*ii*) that the jumping occurs at a later instant and with having the system's vertical displacement reduced. Such an outcome makes us confident that we can continue using our framework to carry out a systematic analysis of the influence of geometrical and wetting properties of pillars on the behavior of a particle-droplet system.

3.2. Grid independence study

We have already validated the numerical framework in the time domain in our previous studies [27,37], and we note that we have neither experienced difficulties nor limitations in that domain for all our simulations (irrespective of whether we deal with planar or pillared surfaces). We use a constant time step which retains the Courant number below 0.5 for the duration of the computations. We also demonstrated spatial convergence of our simulations on planar surfaces [37]. It is now needed to prove spatial convergence in the cases where pillars are introduced. We have varied the grid resolution in the vicinity of the pillars and first we want to find out if we can reach satisfactory results using a default configuration of our framework. The default grid has 40 cells per droplet radius (also the simulation presented in Fig. 1). We have then tested a coarser mesh with 30 cells per droplet radius for the simulations on our benchmark surface (S1), with the following argument: since for that surface the size of the pillars is the smallest of all the configurations used, we argue that if a simulation is grid independent for that case, the same can be said for the cases when larger pillars are used.

In the higher resolution case (40 cells per radius), the pillars are resolved with 4.65 cells per pillar side, whereas for the 30 cells per radius case the same resolution reduces to 3.5 cells. In Fig. 2 we present variations of the different components of the kinetic energy for the

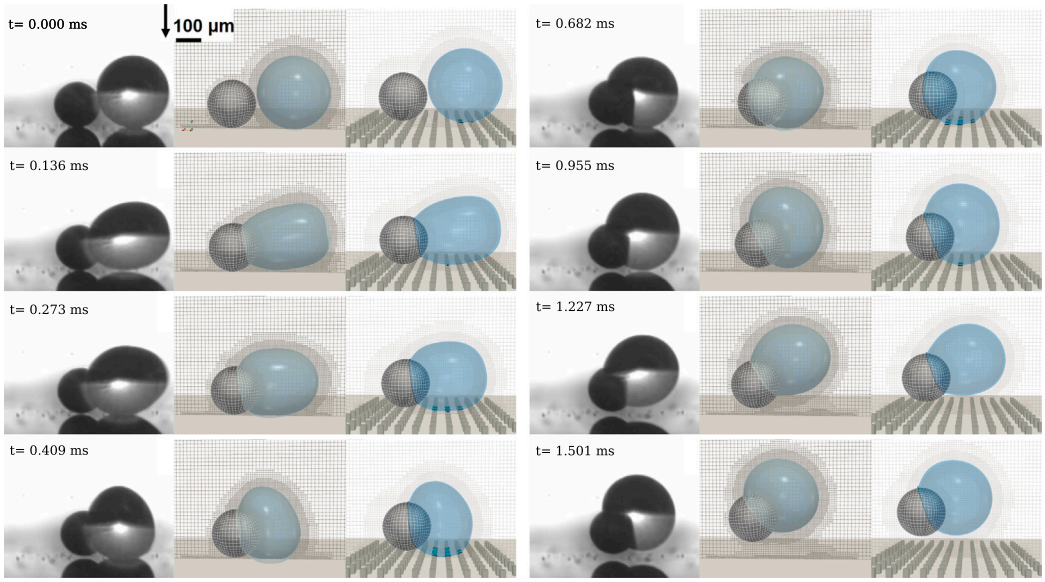

Fig. 1. Particle-droplet coalescence and jumping - comparison between experimental observations by Yan et al. [36] (left column), numerical results by Konstantinidis et al. [37] using a planar superhydrophobic surface and the contact angle $\theta_{eq} = 170°$(middle column), and the numerical results from the present work using the microstructured (pillared) substrate S1 with an intrinsic contact angle $\theta_{eq} = 105°$ (right column). Evolution takes place top to bottom, column wise, with the corresponding instants indicated row-wise for the three types of results. The droplet has a radius $R_d = 120$ μm (right object) and the particle $R_p = 80$ μm (left object). The top left image shows the gravitational vector with a black arrow. The experimental images are reprinted (adapted) with permission from ACS Nano 16, 8 (2022). Copyright 2022 American Chemical Society, whereas the numerical images for the middle columns are reprinted (adapted) with permission from Physics of Fluids 36, 8 (2024). Copyright 2024 AIP Publishing.

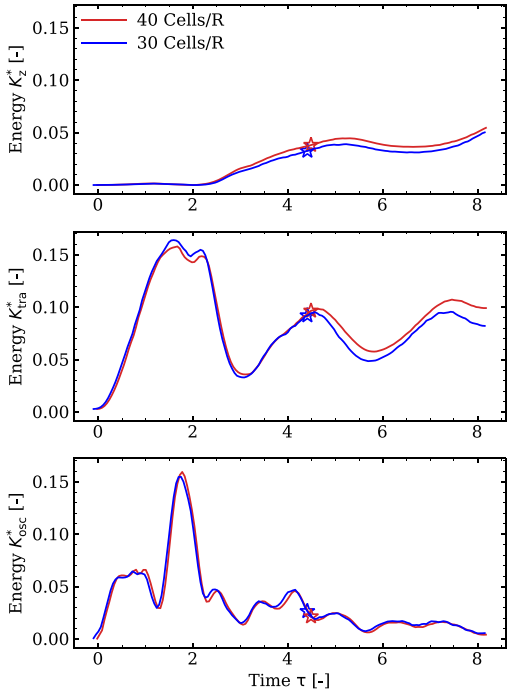

Fig. 2. Different components of kinetic energy for surface S1 (vertical in z direction for the system (top figure), the summed droplet and particle translational energy (middle figure) and the droplet's oscillating energy (K^*_{tot} - K^*_{tra})), (bottom figure) for the coarse and the refined mesh with the resolutions of 30 and 40 cells/R_d, respectively. The components are normalized by the total released surface energy. The asterisk symbols indicate the moment of particle-droplet jumping in the respective cases.

two grids. The components are the kinetic energy of the system in the vertical z-direction (translational energy), followed by the sum of the translational kinetic energies of the droplet-particle system and, finally, the oscillational energy of the droplet (the kinetic energy minus the translational kinetic energy). There is a great agreement between the two simulations, which permits us to go ahead with our investigations using our default grid with 40 cells per droplet radius. Although it may appear tempting to use a coarser mesh for the simulations, we argue that using the finer one will provide even more trustworthy representations of the flow fields between the pillars, and thus achieve a better understanding of the dissipative mechanisms in that region.

4. Results and discussion

4.1. Particle-droplet coalescence and jumping from a pillared surface

We start the analysis by comparing the behavior of a particle-droplet system during coalescence and jumping from the planar surface (extremely homogeneous, with a very low degree of hysteresis) and the microstructured (pillared) surface S1. When working with planar surfaces, the jumping velocity (or energy) is often connected to the apparent contact angle that a stationary droplet has on a superhydrophobic surface, both for droplet-droplet jumping and particle-droplet jumping. For pillared surfaces, we note again that we have selected their geometrical and wetting properties by looking at available experimental publications and taking similar pillar sizes (in relation to droplet radius) and solid areas, while in the same time facilitating a comparison between the processes on those and planar surfaces. In Figs. 3 and 4 we compare the kinetic energies and the available surface energy for the two types of substrates. Fig. 3 demonstrates that the upwards velocity and the kinetic energy of the jumping particle-droplet aggregate are lower on the pillared surface S1 than those on a planar surface (with $\theta_{eq} = 170°$). For the former surface, the detachment of the particle-droplet system takes place later, with the correct capturing of the trends related to the droplet oscillation sequences throughout the process. We also note that the patterns of the particle and droplet motions show strong resemblance for the two types of surfaces.

The results shown in Fig. 4 also point out to the decrease in both cases of the total contact area of the droplet to the substrate. We have also verified that no changes are observed for the particle-substrate contact area. For both surfaces, the sequence of events qualitatively looks the same: when a droplet initiates spreading to a hydrophilic particle, it displaces itself towards the particle and the created liquid

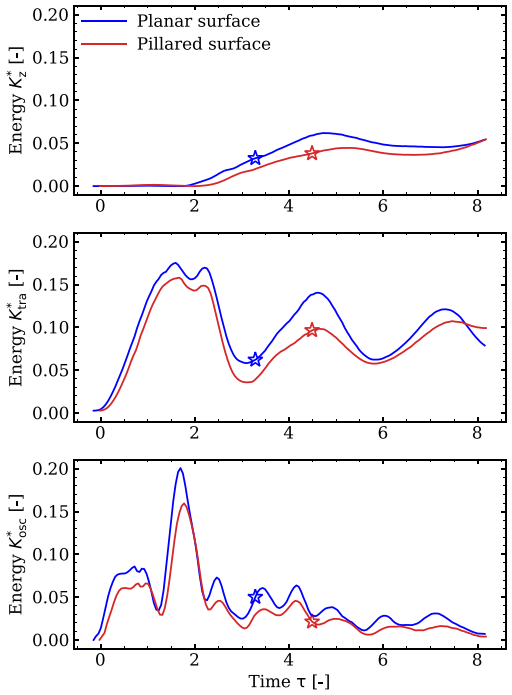

Fig. 3. Different components of kinetic energy for a particle-droplet system - comparison between the numerical results obtained for planar and pillared surfaces (S1). The components are the same as those shown in Fig. 2. The asterisk symbols indicate the moment of jumping.

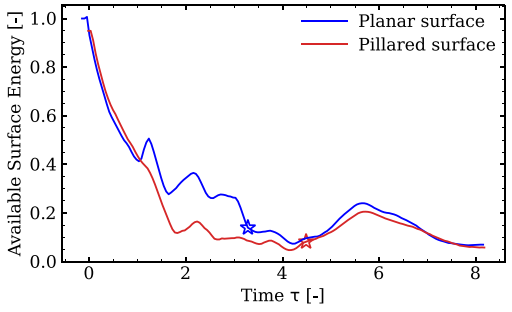

Fig. 4. Surface energy of the system for the planar and pillared substrates, as computed from the free interface between the droplet and the gas and from the contact interfaces between the droplet and the particle or substrate. The values are normalized by the total released surface energy. The asterisk symbols indicate the moment of jumping. In the early phase of the process, energy is decreased at same rate, but afterwards the droplet acting on the planar surface recovers surface energy more efficiently than that on the pillared surface.

bridge interacts with a substrate. Then, the droplet alternates between prolate and oblate shapes and experiences an expansion of its contact area with the substrate. When comparing the available surface energy at different instants between the two surfaces, the planar surface case has a larger contact area in relation to the structured surface. With a highly efficient superhydrophobic surface as the one used in the study of Yan et al. [21], this area is considered to provide additional surface energy which will be then given back to the droplet during the retraction and detachment steps. Conversely, the microstructures of pillared surfaces and having a lower intrinsic contact angle will not return this energy in the same way. Such surfaces facilitate an increase of the liquid-gas interface area due to the presence of the pillars, and the surface energy will be released at a later stage of the adhesion process of the droplet to the particle. We argue that this reduction of the available surface energy at least partly explains the increased dissipation of the kinetic energy in the pillared configuration cases.

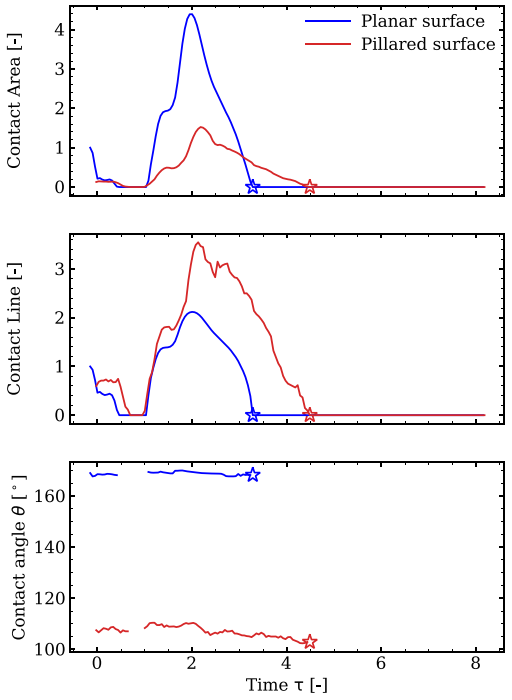

Fig. 5. Evolution of contact parameters between the droplet and the substrate for the two types of surfaces (planar and the pillared surface S1). The figures show the normalized contact areas (top), the normalized total contact lines (middle) and the averaged dynamic contact angles imposed in the vicinity of the contact line (bottom). The calculated contact area and the length of the contact line are normalized by the initial wetting area and contact line length of a static droplet on a homogeneous planar surface. The asterisk symbols indicate the moment of jumping.

In Fig. 5 we compare the contact areas of the droplet with the two substrates (top figure). The contact areas are normalized by the initial wetting area that a sessile droplet of the same size would have when residing on a homogeneous planar surface. In addition, we show the cumulative length of the contact lines for the two cases (figure in the middle) and the plot of the contact angle values as adopted at the contact line location for each cell and averaged across the contact line (bottom figure). With the latter figure we want to show the relative influence of the advancing and receding motions. We observe that the microstructured surface has a reduced maximum contact area since, in that case, the droplet is in contact with only the top of the pillars. On the other hand, the planar surface has a more pronounced expansion of the contact area, but facilitates retraction of that area at a higher rate and thus makes it possible for the particle-droplet system to detach earlier from the surface. We also note that the contact line was measured significantly longer for the pillared substrate. The properties of the contact line strongly influence the capillary forces at the triple-phase contact, with the length of that line being connected to higher viscous dissipation at the contact line. We see that the contact angles for the two surfaces are rather different, even if a dynamic contact-angle representation is implemented for both cases. In addition, no significant variations are observed for the spreading and jumping stages, with the trends of the evolution of the system parameters being consistent. We argue that regarding the type of the contact angle the advancing mode is a dominant one in the entire process, as compared to the receding motion of the contact line.

4.2. Influence of geometrical properties of pillars

4.2.1. Variation of width of pillars and of solid area fraction

We here look at the influence of geometrical properties of the pillars on the coalescence and jumping process, where we work with a series

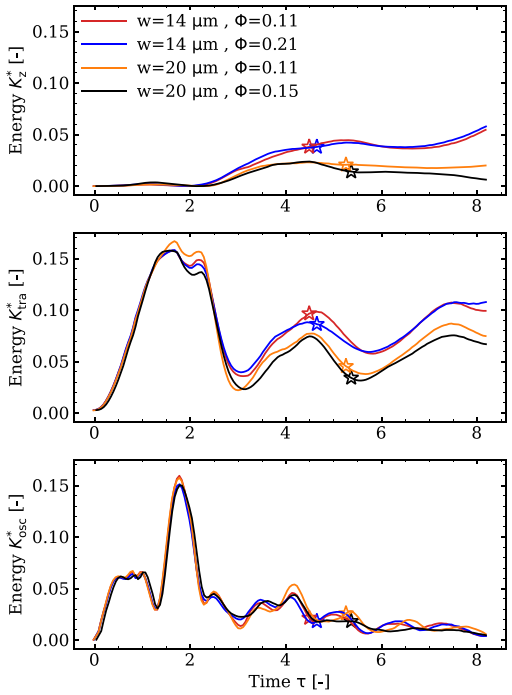

Fig. 6. Different components of kinetic energy for a particle-droplet system for S1–S4 (see Table 1). The components are the same as those shown in Fig. 2. The energy is dissipated primarily due to the increase of the width of the pillars, with a reduced influence of the pitch sizes. The asterisk symbols indicate the moment of jumping.

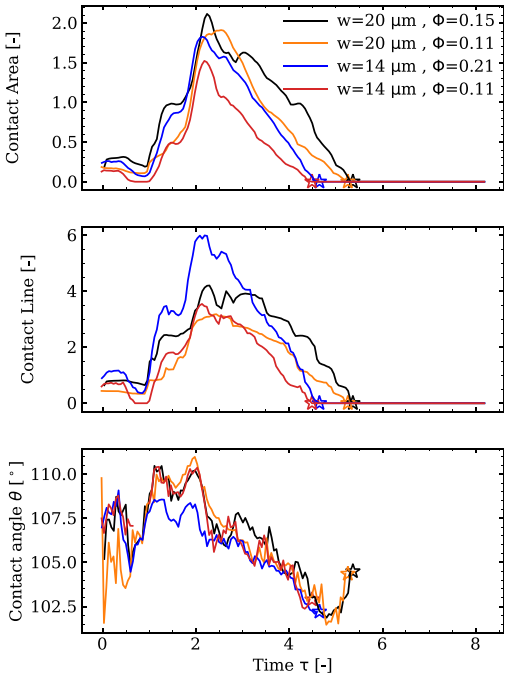

Fig. 7. Evolution of contact parameters between the droplet and substrate for substrates S1–S4. The figures show the normalized contact area (top), the normalized total contact lines (middle) and the averaged dynamic contact angles imposed in the vicinity of the contact line (bottom). The calculated contact area and the length of the contact line are normalized by the initial wetting area and contact line length of a static droplet on a homogeneous planar surface. The asterisk symbols indicate the moment of jumping.

of configurations regarding their location and cross-section area. The surface S1 has the width of $w = 14$ μm and pitch of $s = 28$ μm. These dimensions correspond to $w = 4.65$ cells and $s = 9.35$ cells in the current grid configuration, while the solid area fraction is $\Phi = 0.11$. The results for S1 are compared to those from the following substrates: the substrate S2 with $w = 14$ μm and $\Phi = 0.21$, the substrate S3 with $w = 20$ μm (or 6.65 cells) and $\Phi = 0.11$ and the substrate S4 with $w = 20$ μm and $\Phi = 0.15$. Our findings are best demonstrated when looking at Figs. 6 and 7 together. In Fig. 6 we present for the different configurations the evolution of the total upwards translational kinetic energy of the system (top), the summed droplet-particle translational kinetic energy (middle) and the oscillatory kinetic energy of the droplet (bottom). In Fig. 7 we show the evolution of the contact area and corroborate an expectation that increasing the width of the pillars increases the droplet-substrate wetting area. When we combine the latter observation with the reduction in the jumping energy for wider pillars (see Fig. 6), we argue that the total dissipation in the system has increased in such cases. Observations from looking at different instants in the simulations suggest that wider pillars increase the area of the side contact for the substrates with the same solid area fraction Φ. Finally, our results show that increasing the size of the pitch (and thereby reducing the solid area fraction) has a rather limited effect on the jumping energy, although a small increase in that energy is observed for the substrates having larger valleys/grooves.

4.2.2. *Influence of height of pillars*

We want to see here whether the presence of pillars influences differently the Cassie-Baxter behavior of a sessile droplet from that involving a particle-droplet coalescence and jumping. Namely, with the former it is likely that the height of the pillars does not influence the droplet behavior. On the other hand, one would expect that in dynamic situations, such as a droplet impact on a pillared surface or coalescence-induced droplet jumping from a microstructured surface, there exists an effect of the pillar height. To quantify this effect on our particle-droplet system, we introduce the new configuration S5, the same as S3

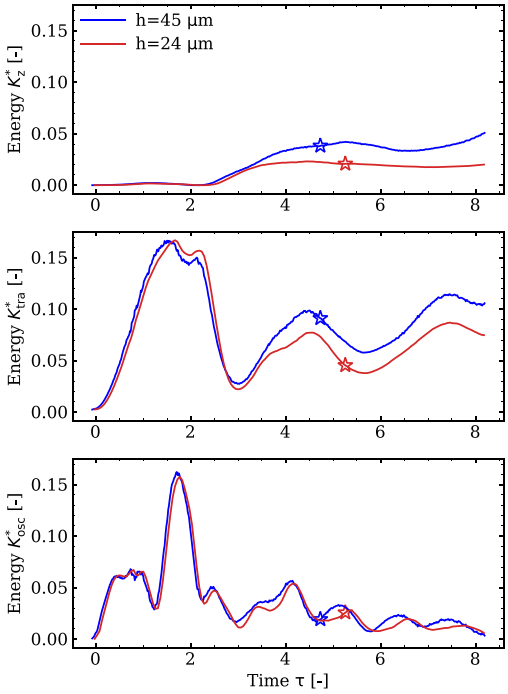

Fig. 8. Different components of kinetic energy for a particle-droplet system - comparison between the results obtained for substrates S3 and S5 with different pillar heights (see Table 1). The components are the same as in Fig. 2. The energies are normalized by the total released surface energy. The case with higher pillars promotes the superhydrophobic nature of the surface and facilitates the particle-droplet system to jump higher. The asterisk symbols indicate the moment of jumping.

but with elongated pillars (see Table 1). The energy budgets for the two substrates are presented in Fig. 8. When the pillars are elongated from $h = 24$ μm to $h = 45$ μm, the upwards kinetic energy (top

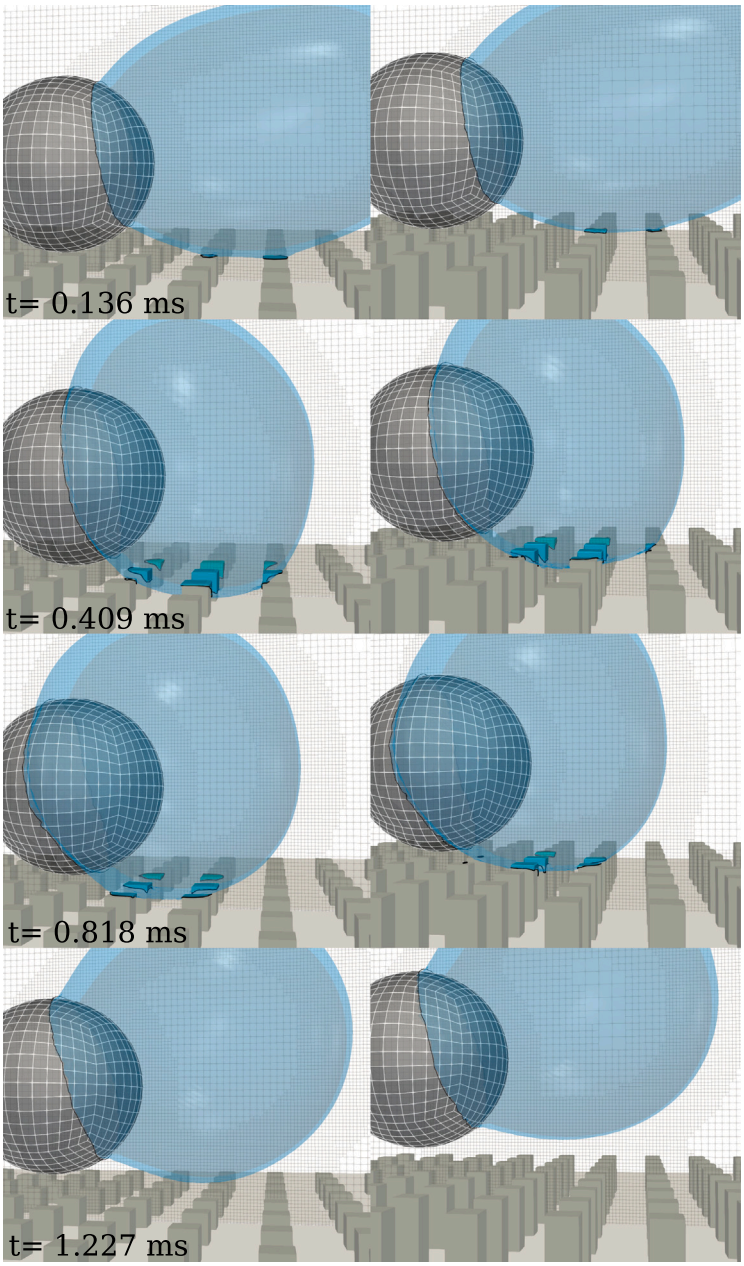

Fig. 9. Three-dimensional close-up visualization of the droplet spreading on the particle and the subsequent particle-droplet jumping for substrates S3 (left column) and S5 (right column) with different pillar heights (see Table 1). The wetted area on top and along the side of the pillars is highlighted, and the apparent contact line is given in black color. (For interpretation of the references to color in this figure legend, the reader is referred to the web version of this article.)

figure) suggests an increased degree of dissipation for shorter pillars. We argue that in this dynamical case the interaction with the side of the pillars and the bottom of the surface will have a significant effect. Such a conclusion holds below a certain threshold above which the pillar height will again become of lesser importance.

A series of instants presented in Fig. 9 show the variations for the two substrates in the contact formations during different oscillatory shapes of the spreading droplet. We emphasize here the liquid penetration at the side of the pillars for the case with the higher pillars. The contact angle calculated at the contact line, including the situations when the contact line resides on the side of a pillar, is also presented in Fig. 10. In addition, we notice the larger contact area and the contact line for the substrate S5 during the wetting phase. On the other hand, the same substrate experiences a higher rate of dewetting, as observed in the contact area evolution and before the jumping instant. These observations are connected to the reduced influence of the bottom of the grooves for the case with the higher pillars. As a result, the duration of the droplet-substrate attachment before the jumping takes place is connected to the ability of the interface to penetrate the area between pillars and to regain a higher velocity during dewetting, thus neglecting the possible pressure interaction due to the presence of the bottom wall.

4.3. Influence of contact angle

Having gone through the different scenarios related to the jumping energy and contact parameters for the particle-droplet system when different geometric properties for the structured surfaces are used, we now focus on the influence of the intrinsic contact angle. For that purpose, the contact angles implemented in the configuration S6 are reduced by 15° comparing to those used for S1. We are particularly interested in whether such a change will facilitate a transition from the Cassie-Baxter to the Wenzel wetting behavior. With the latter, we

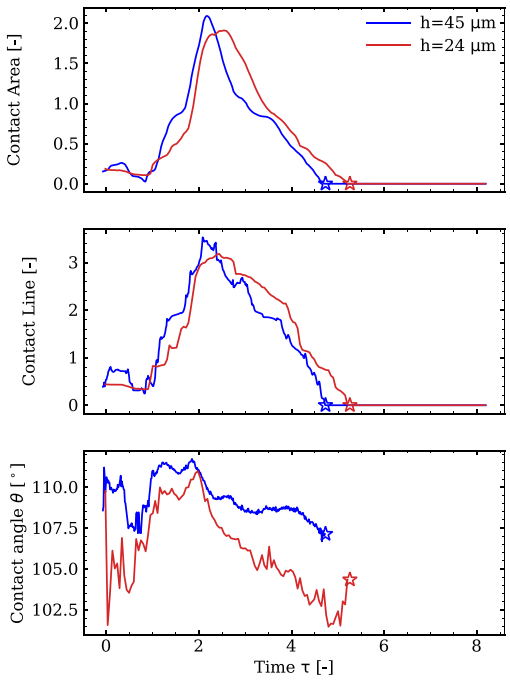

Fig. 10. Evolution of contact parameters between the droplet and the substrate for substrates S3 and S5 with different pillar heights (see Table 1). The plots show the normalized contact area (top), the normalized total contact line (middle) and the averaged dynamic contact angle imposed in the vicinity of the contact line (bottom). The calculated contact area and the length of the contact line are normalized by the initial wetting area and contact line length of a static droplet on a homogeneous planar surface. The asterisk symbols indicate the moment of jumping.

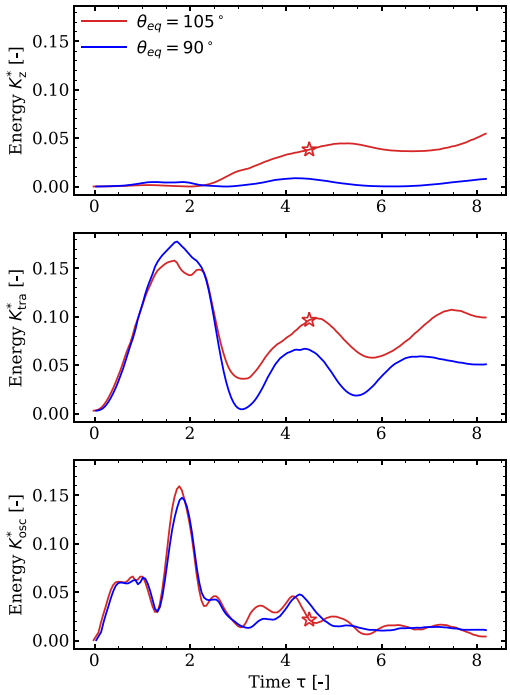

Fig. 11. Different components of kinetic energy for a particle-droplet system - comparison between the results obtained for substrates S1 and S6 with different intrinsic contact angles (see Table 1). The components are the same as in Fig. 2. The energies are normalized by the total released surface energy. When $\theta = 90°$ there is no jumping of the system and the translational energy is dissipated at a significantly higher rate compared to that for the substrate S1. The asterisk symbols indicate the moment of jumping.

expect that the bottom of the structured surface will almost be fully wetted already during the spreading of the droplet to the particle. As a result, the dissipation of energy increases from the excess wetting area and the resulting interaction of the droplet with the surrounding pillars. The gained upwards kinetic energy from the interaction of the oscillatory droplet with the substrate S6 is not sufficient to overcome the droplet-surface adhesive forces, and, consequently, the particle-droplet system will not jump in this case. In Fig. 11 we show how the energy of the system for the substrate S6 is dissipated in such a way that there is almost no upwards momentum whatsoever, as compared to the case with the substrate S1.

These observations appear even more straightforward when looking at the results presented in Figs. 12 and 13. The figures show zoomed-in and the absolute values of the wetted area for the two substrates. The extent of penetration of the droplet (and thus the transition to a Wenzel state) between the pillars for the substrate S6 makes it not possible to overcome the adhesive forces, and we see that the droplet-surface contact area is increased three-fold in that case (Fig. 13, top). The average contact angle, that is implemented by using the dynamic Kistler model, appears in advancing motion slightly above 90 degrees for most of the simulation, approximately 15° less than the default case (substrate S1). We note here that in order to identify a threshold value of an intrinsic contact angle when the transition between the states happens, further studies are required not only dealing with a combination of contact angles with the configuration of pillars, but also taking into consideration the droplet and particle characteristic dimensions. These dimensions play an important role when characterizing the capillary-inertial forces, which dictate the dynamics of spreading and, therefore, govern the penetration of the droplet to a structured surface in a very dynamic process such as the one of particle–droplet coalescence and jumping.

5. Conclusions

We have carried out a multiphase direct numerical study of particle-droplet coalescence and jumping from a series of microstructured superhydrophobic substrates with rectangular pillars. We have used a combined volume of fluid-immersed boundary framework, introduced a systematic variation of geometrical and wetting properties of the pillars and studied their combined effects on a number of identified scenarios of the particle-droplet behavior on microstructured surfaces. We have varied width and height of the pillars, pitch between them (thus governing the total solid area fraction) and their contact angles.

Our findings confirm that the chosen microstructured surfaces behave in a similar quantitative and qualitative way as do homogeneous planar surfaces with significantly higher intrinsic contact angles. Our simulations on pillared surfaces have been able to reproduce correct dynamics of all relevant stages of the particle-droplet coalescence and jumping process: (*i*) initial spreading of the droplet on the particle and creation of a liquid bridge, (*ii*) variations of droplet shape during its spreading on the particle and (*iii*) departure of the particle-droplet system from a microstructured surface.

Within the chosen parameter space, we have quantified energy efficiencies and dissipation and made comparisons between fundamental features of the process on microstructured and planar homogeneous surfaces. On former surfaces, detachment of the particle-droplet system takes place later than that on planar superhydrophobic surfaces. We have identified width and height of the pillars as important geometrical properties that affect efficiency of the process, whereas a reduced effect has been found of the distance between the pillars. In general, we have shown how the presence of rectangular pillars affects the energy dissipation, causing a decreased upwards momentum of the particle-droplet system for all the tests made with the pillared surfaces. We have also studied a transition between Cassie-Baxter and Wenzel wetting states by reducing the intrinsic contact angles of the pillars. We have shown and explained why the particle-droplet system does not jump when the Wenzel wetting state is reached.

In the future we plan to focus on exploring additional types of structures such as hill-like features or grooves and to consider the flexibility of the structures as possible ways to achieve higher efficiency utilizing the particle-droplet jumping phenomenon.

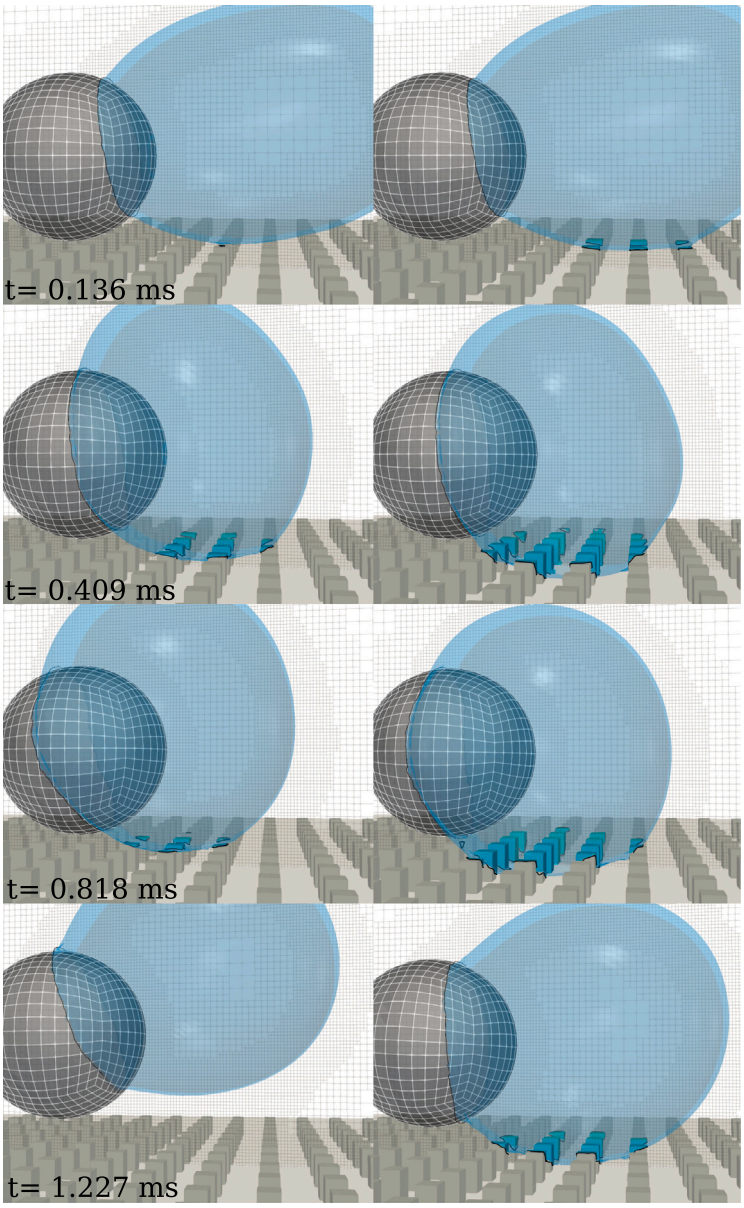

Fig. 12. Three-dimensional close-up visualizations of the droplet spreading on the particle and the subsequent jumping (only for the left column!) for substrates S1 (left) and S6 (right) with different intrinsic contact angles (see Table 1). The interface in contact between the droplet and the substrate is highlighted, and the apparent contact line is given in black color (right column). (For interpretation of the references to color in this figure legend, the reader is referred to the web version of this article.)

CRediT authorship contribution statement

Konstantinos Konstantinidis: Writing – review & editing, Writing – original draft, Visualization, Validation, Software, Methodology, Formal analysis, Data curation, Conceptualization. **Johan Göhl:** Writing – review & editing, Visualization, Validation, Software, Methodology, Investigation, Formal analysis. **Andreas Mark:** Writing – review & editing, Visualization, Validation, Supervision, Software, Resources, Methodology, Investigation, Funding acquisition, Formal analysis. **Xiao Yan:** Writing – review & editing, Visualization, Validation, Resources, Investigation, Formal analysis. **Nenad Miljkovic:** Formal analysis, Investigation, Resources, Validation, Visualization, Writing – review & editing. **Srdjan Sasic:** Writing – review & editing, Visualization, Validation, Supervision, Resources, Project administration, Methodology, Investigation, Funding acquisition, Formal analysis, Conceptualization.

Declaration of competing interest

The authors declare that they have no known competing financial interests or personal relationships that could have appeared to influence the work reported in this paper.

Acknowledgments

The authors would like to acknowledge the financial support of this project by the Swedish Research Council (Vetenskapsrådet, no. 2019-04969). In addition, it is acknowledged that the handling of data and other computations were enabled by resources provided by the National Academic Infrastructure for Supercomputing in Sweden (NAISS), partially funded by the Swedish Research Council through grant agreement no. 2022-06725.

Appendix A. Supplementary data

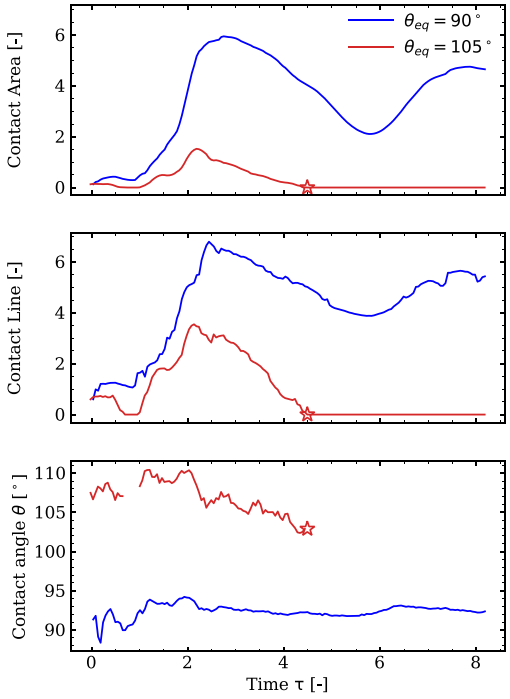

Fig. 13. Evolution of contact parameters between the droplet and the substrate for substrates S1 and S6 with different intrinsic contact angles. The plots show the normalized contact area (top), the normalized total contact line (middle) and the averaged dynamic contact angle imposed in the vicinity of the contact line (bottom). The calculated contact area and the length of the contact line are normalized by the initial wetting area and contact line length of a static droplet on a homogeneous planar surface. The asterisk symbols indicate the moment of jumping.

- Video visualization of the coalescence and jumping of a water droplet with radius of $R_d = 120$ μm merging with a spherical solid particle $R_p = 80$ μm for the case with substrate S1. The video frame-rate is 5 fps, the time interval between frames is $t_{int} = 0.00789$ ms and the total duration of the simulation is $t_{tot} = 1.64$ ms.

Supplementary material related to this article can be found online at https://doi.org/10.1016/j.surfin.2025.106333.

Data availability

Data will be made available on request.

References

[1] Y.C. Jung, B. Bhushan, Dynamic effects of bouncing water droplets on superhydrophobic surfaces, Langmuir 24 (12) (2008) 6262–6269, http://dx.doi.org/10.1021/la8003504, URL https://pubs.acs.org/doi/10.1021/la8003504.

[2] S. Nishimoto, B. Bhushan, Bioinspired self-cleaning surfaces with superhydrophobicity, superoleophobicity, and superhydrophilicity, RSC Adv. 3 (3) (2013) 671–690, http://dx.doi.org/10.1039/c2ra21260a.

[3] K.M. Wisdom, J.A. Watson, X. Qu, F. Liu, G.S. Watson, C.-H. Chen, Self-cleaning of superhydrophobic surfaces by self-propelled jumping condensate, Proc. Natl. Acad. Sci. 110 (20) (2013) 7992–7997, http://dx.doi.org/10.1073/PNAS.1210770110, URL https://www.pnas.org/content/110/20/7992 https://www.pnas.org/content/110/20/7992.abstract.

[4] J.B. Boreyko, C.P. Collier, Delayed frost growth on jumping-drop superhydrophobic surfaces, ACS Nano 7 (2) (2013) 1618–1627, http://dx.doi.org/10.1021/NN3055048, URL https://pubs.acs.org/doi/full/10.1021/nn3055048.

[5] X. Li, C. Ma, T. Shi, H. Yang, C. Zhang, W. Qi, C. Li, R. Liu, W. He, Y. Liu, Waterborne robust superhydrophobic pfdtes@tio2-PU coating with stable corrosion resistance, long-term environmental adaptability, and delayed icing functions on Al–Li alloy, J. Mater. Res. Technol. 32 (2024) 3357–3370, http://dx.doi.org/10.1016/j.jmrt.2024.08.131, URL https://linkinghub.elsevier.com/retrieve/pii/S2238785424019215.

[6] K.S. Boyina, A.J. Mahvi, S. Chavan, D. Park, K. Kumar, M. Lira, Y. Yu, A.A. Gunay, X. Wang, N. Miljkovic, Condensation frosting on meter-scale superhydrophobic and superhydrophilic heat exchangers, Int. J. Heat Mass Transfer 145 (2019) 118694, http://dx.doi.org/10.1016/j.ijheatmasstransfer.2019.118694.

[7] N. Miljkovic, R. Enright, E.N. Wang, Effect of droplet morphology on growth dynamics and heat transfer during condensation on superhydrophobic nanostructured surfaces, ACS Nano 6 (2) (2012) 1776–1785, http://dx.doi.org/10.1021/nn205052a.

[8] R. Enright, N. Miljkovic, N. Dou, Y. Nam, E.N. Wang, Condensation on superhydrophobic copper oxide nanostructures, J. Heat Transf. 135 (9) (2013) http://dx.doi.org/10.1115/1.4024424, URL https://asmedigitalcollection.asme.org/heattransfer/article/135/9/091304/366655/Condensation-on-Superhydrophobic-Copper-Oxide https://asmedigitalcollection.asme.org/heattransfer/article/doi/10.1115/1.4024424/366655/Condensation-on-Superhydrophobic-Copper-.

[9] W. Barthlott, C. Neinhuis, Purity of the sacred lotus, or escape from contamination in biological surfaces, Planta 202 (1) (1997) 1–8, http://dx.doi.org/10.1007/S004250050096, URL https://link.springer.com/article/10.1007/s004250050096.

[10] L. Feng, Y. Zhang, J. Xi, Y. Zhu, N. Wang, F. Xia, L. Jiang, Petal effect: A superhydrophobic state with high adhesive force, Langmuir 24 (8) (2008) 4114–4119, http://dx.doi.org/10.1021/la703821h.

[11] C. Lv, P. Hao, Z. Yao, Y. Song, X. Zhang, F. He, Condensation and jumping relay of droplets on lotus leaf, Appl. Phys. Lett. 103 (2) (2013) 1–5, http://dx.doi.org/10.1063/1.4812976.

[12] C.W. Extrand, S.I. Moon, Repellency of the lotus leaf: Contact angles, drop retention, and sliding angles, Langmuir 30 (29) (2014) 8791–8797, http://dx.doi.org/10.1021/la5019482, URL https://pubs.acs.org/doi/full/10.1021/la5019482.

[13] C. Yu, S. Sasic, K. Liu, S. Salameh, R.H. Ras, J.R. van Ommen, Nature–Inspired self–cleaning surfaces: Mechanisms, modelling, and manufacturing, Chem. Eng. Res. Des. 155 (2020) 48–65, http://dx.doi.org/10.1016/j.cherd.2019.11.038, URL https://linkinghub.elsevier.com/retrieve/pii/S0263876219305702.

[14] C.W. Extrand, Criteria for ultralyophobic surfaces, Langmuir 20 (12) (2004) 5013–5018, http://dx.doi.org/10.1021/LA036481S, URL https://pubs.acs.org/doi/full/10.1021/la036481s.

[15] D. Wang, Q. Sun, M.J. Hokkanen, C. Zhang, F.Y. Lin, Q. Liu, S.P. Zhu, T. Zhou, Q. Chang, B. He, Q. Zhou, L. Chen, Z. Wang, R.H. Ras, X. Deng, Design of robust superhydrophobic surfaces, Nature 582 (7810) (2020) 55–59, http://dx.doi.org/10.1038/s41586-020-2331-8.

[16] Y. Sun, Y. Jiang, C.-H. Choi, G. Xie, Q. Liu, J.W. Drelich, Direct measurements of adhesion forces for water droplets in contact with smooth and patterned polymers, Surf. Innov. 6 (1–2) (2017) 1–52, http://dx.doi.org/10.1680/jsuin.17.00049, URL https://drive.google.com/file/d/1JLk1ljiFcx7Nesz9JP5cK6adDtHwTGGW/view?usp=embed{_}facebook http://www.icevirtuallibrary.com/doi/10.1680/jsuin.17.00049.

[17] D. Öner, T.J. McCarthy, Ultrahydrophobic surfaces. Effects of topography length scales on wettability, Langmuir 16 (20) (2000) 7777–7782, http://dx.doi.org/10.1021/la000598o, URL https://pubs.acs.org/doi/abs/10.1021/la000598o.

[18] A.B. Cassie, S. Baxter, Wettability of porous surfaces, Trans. Faraday Soc. 40 (1944) 546–551, http://dx.doi.org/10.1039/TF9444000546, URL https://pubs.rsc.org/en/content/articlehtml/1944/tf/tf9444000546 https://pubs.rsc.org/en/content/articlelanding/1944/tf/tf9444000546.

[19] D. Bonn, J. Eggers, J. Indekeu, J. Meunier, Wetting and spreading, Rev. Modern Phys. 81 (2) (2009) 739–805, http://dx.doi.org/10.1103/RevModPhys.81.739.

[20] M.D. Mulroe, B.R. Srijanto, S.F. Ahmadi, C.P. Collier, J.B. Boreyko, Tuning superhydrophobic nanostructures to enhance jumping-droplet condensation, ACS Nano 11 (8) (2017) 8499–8510, http://dx.doi.org/10.1021/acsnano.7b04481, URL https://pubs.acs.org/doi/10.1021/acsnano.7b04481.

[21] X. Yan, L. Zhang, S. Sett, L. Feng, C. Zhao, Z. Huang, H. Vahabi, A.K. Kota, F. Chen, N. Miljkovic, Droplet jumping: Effects of droplet size, surface structure, pinning, and liquid properties, ACS Nano 13 (2) (2019) 1309–1323, http://dx.doi.org/10.1021/ACSNANO.8B06677, URL https://pubs.acs.org/doi/abs/10.1021/acsnano.8b06677.

[22] J.B. Boreyko, C.H. Chen, Self-propelled dropwise condensate on superhydrophobic surfaces, Phys. Rev. Lett. 103 (18) (2009) 2–5, http://dx.doi.org/10.1103/PhysRevLett.103.184501.

[23] F. Liu, G. Ghigliotti, J.J. Feng, C.-H. Chen, Numerical simulations of self-propelled jumping upon drop coalescence on non-wetting surfaces, J. Fluid Mech. 752 (2014) 39–65, http://dx.doi.org/10.1017/jfm.2014.320, URL https://www.cambridge.org/core/product/identifier/S0022112014003206/type/journal{_}article.

[24] R. Enright, N. Miljkovic, J. Sprittles, K. Nolan, R. Mitchell, E.N. Wang, How coalescing droplets jump, ACS Nano 8 (10) (2014) 10352–10362, http://dx.doi.org/10.1021/nn503643m.

[25] R. Mukherjee, H.A. Gruszewski, L.T. Bilyeu, D.G. Schmale, J.B. Boreyko, Synergistic dispersal of plant pathogen spores by jumping-droplet condensation and wind, Proc. Natl. Acad. Sci. 118 (34) (2021) e2106938118, http://dx.doi.org/10.1073/pnas.2106938118.

[26] Y. Li, H. Zhang, J. Du, Q. Min, X. Wu, L. Sun, Coalescence-induced self-propelled particle transport with asymmetry arrangement, ACS Appl. Mater. Interfaces (2024) http://dx.doi.org/10.1021/ACSAMI.4C01355, URL https://pubs.acs.org/doi/full/10.1021/acsami.4c01355.

[27] K. Konstantinidis, J. Göhl, A. Mark, S. Sasic, Coalescence-induced jumping of droplets from superhydrophobic surfaces—The effect of contact-angle hysteresis, Phys. Fluids 34 (11) (2022) 113302, http://dx.doi.org/10.1063/5.0118645, URL https://aip.scitation.org/doi/10.1063/5.0118645.

[28] R. Attarzadeh, A. Dolatabadi, Coalescence-induced jumping of micro-droplets on heterogeneous superhydrophobic surfaces, Phys. Fluids 29 (1) (2017) 012104, http://dx.doi.org/10.1063/1.4973823, URL http://aip.scitation.org/doi/10.1063/1.4973823.

[29] F. Chu, X. Yan, N. Miljkovic, How superhydrophobic grooves drive single-droplet jumping, Langmuir 38 (14) (2022) 4452–4460, http://dx.doi.org/10.1021/acs.langmuir.2c00373, URL https://pubs.acs.org/doi/full/10.1021/acs.langmuir.2c00373.

[30] R. Mukherjee, A.S. Berrier, K.R. Murphy, J.R. Vieitez, J.B. Boreyko, How surface orientation affects jumping-droplet condensation, Joule 3 (5) (2019) 1360–1376, http://dx.doi.org/10.1016/j.joule.2019.03.004.

[31] X. Yan, Z. Huang, S. Sett, J. Oh, H. Cha, L. Li, L. Feng, Y. Wu, C. Zhao, D. Orejon, F. Chen, N. Miljkovic, Atmosphere-mediated superhydrophobicity of rationally designed micro/nanostructured surfaces, ACS Nano 13 (4) (2019) 4160–4173, http://dx.doi.org/10.1021/acsnano.8b09106, URL https://pubs.acs.org/doi/full/10.1021/acsnano.8b09106 https://pubs.acs.org/doi/10.1021/acsnano.8b09106.

[32] S. Farokhirad, T. Lee, Computational study of microparticle effect on self-propelled jumping of droplets from superhydrophobic substrates, Int. J. Multiph. Flow 95 (2017) 220–234, http://dx.doi.org/10.1016/j.ijmultiphaseflow.2017.05.008.

[33] B. Bhushan, Y.C. Jung, Wetting, adhesion and friction of superhydrophobic and hydrophilic leaves and fabricated micro/nanopatterned surfaces, J. Phys.: Condens. Matter. 20 (22) (2008) 225010, http://dx.doi.org/10.1088/0953-8984/20/22/225010, URL https://iopscience.iop.org/article/10.1088/0953-8984/20/22/225010 https://iopscience.iop.org/article/10.1088/0953-8984/20/22/225010/meta.

[34] W. Choi, A. Tuteja, J.M. Mabry, R.E. Cohen, G.H. McKinley, A modified cassie–Baxter relationship to explain contact angle hysteresis and anisotropy on non-wetting textured surfaces, J. Colloid Interface Sci. 339 (1) (2009) 208–216, http://dx.doi.org/10.1016/J.JCIS.2009.07.027.

[35] A.T. Paxson, K.K. Varanasi, Self-similarity of contact line depinning from textured surfaces, Nat. Commun. 4 (1) (2013) 1492, http://dx.doi.org/10.1038/ncomms2482, URL https://www.nature.com/articles/ncomms2482.

[36] X. Yan, B. Ji, L. Feng, X. Wang, D. Yang, K.F. Rabbi, Q. Peng, M.J. Hoque, P. Jin, E. Bello, S. Sett, M. Alleyne, D.M. Cropek, N. Miljkovic, Particulate-droplet coalescence and self-transport on superhydrophobic surfaces, ACS Nano 16 (8) (2022) 12910–12921, http://dx.doi.org/10.1021/acsnano.2c05267, URL https://pubs.acs.org/doi/10.1021/acsnano.2c05267.

[37] K. Konstantinidis, J. Gohl, A. Mark, X. Yan, N. Miljkovic, S. Sasic, Particle-droplet coalescence and jumping on superhydrophobic surfaces—A direct numerical simulations study, Phys. Fluids 36 (8) (2024) 82117, http://dx.doi.org/10.1063/5.0222367, URL /aip/pof/article/36/8/082117/3309947/Particle-droplet-coalescence-and-jumping-on.

[38] W. Xu, C.H. Choi, From sticky to slippery droplets: Dynamics of contact line depinning on superhydrophobic surfaces, Phys. Rev. Lett. 109 (2) (2012) 024504, http://dx.doi.org/10.1103/PHYSREVLETT.109.024504, URL https://journals.aps.org/prl/abstract/10.1103/PhysRevLett.109.024504.

[39] Y. Jiang, C.H. Choi, Droplet retention on superhydrophobic surfaces: A critical review, Adv. Mater. Interfaces 8 (2) (2021) 2001205, http://dx.doi.org/10.1002/ADMI.202001205, URL https://onlinelibrary.wiley.com/doi/full/10.1002/admi.202001205 https://onlinelibrary.wiley.com/doi/abs/10.1002/admi.202001205 https://onlinelibrary.wiley.com/doi/10.1002/admi.202001205.

[40] Y.H. Yeong, A. Milionis, E. Loth, I.S. Bayer, Microscopic receding contact line dynamics on pillar and irregular superhydrophobic surfaces, Sci. Rep. 2015 51 5 (1) (2015) 1–10, http://dx.doi.org/10.1038/srep08384, URL https://www.nature.com/articles/srep08384.

[41] J.U. Brackbill, D.B. Kothe, C. Zemach, A continuum method for modeling surface tension, J. Comput. Phys. 100 (2) (1992) 335–354, http://dx.doi.org/10.1016/0021-9991(92)90240-Y.

[42] A. Mark, B.G. van Wachem, Derivation and validation of a novel implicit second-order accurate immersed boundary method, J. Comput. Phys. 227 (13) (2008) 6660–6680, http://dx.doi.org/10.1016/j.jcp.2008.03.031.

[43] A. Mark, R. Rundqvist, F. Edelvik, Comparison between different immersed boundary conditions for simulation of complex fluid flows, Fluid Dyn. Mater. Process. 7 (3) (2011) 241–258, http://dx.doi.org/10.3970/fdmp.2011.007.241.

[44] S.F. Kistler, Hydrodynamics of wetting, Wettability 6 (1993) 311–430.

[45] J. Göhl, A. Mark, S. Sasic, F. Edelvik, An immersed boundary based dynamic contact angle framework for handling complex surfaces of mixed wettabilities, Int. J. Multiph. Flow 109 (2018) 164–177, http://dx.doi.org/10.1016/j.ijmultiphaseflow.2018.08.001.

[46] K. Washino, H. Tan, M. Hounslow, A. Salman, A new capillary force model implemented in micro-scale CFD–DEM coupling for wet granulation, Chem. Eng. Sci. 93 (2013) 197–205, http://dx.doi.org/10.1016/j.ces.2013.02.006, URL https://linkinghub.elsevier.com/retrieve/pii/S0009250913000973.

[47] G.T. Nguyen, E.L. Chan, T. Tsuji, T. Tanaka, K. Washino, Interface control for resolved CFD-DEM with capillary interactions, Adv. Powder Technol. 32 (5) (2021) 1410–1425, http://dx.doi.org/10.1016/j.apt.2021.03.004, URL https://linkinghub.elsevier.com/retrieve/pii/S0921883121001254.

[48] M. Jiang, B. Zhou, Improvement and further investigation on Hoffman-function-based dynamic contact angle model, Int. J. Hydrog. Energy 44 (31) (2019) 16898–16908, http://dx.doi.org/10.1016/j.ijhydene.2019.04.256.

[49] C. Priest, T.W. Albrecht, R. Sedev, J. Ralston, Asymmetric wetting hysteresis on hydrophobic microstructured surfaces, Langmuir 25 (10) (2009) 5655–5660, http://dx.doi.org/10.1021/la804246a, URL https://pubs.acs.org/doi/10.1021/la804246a.

[50] C. Lv, P. Hao, X. Zhang, F. He, Dewetting transitions of dropwise condensation on nanotexture-enhanced superhydrophobic surfaces, ACS Nano 9 (12) (2015) 12311–12319, http://dx.doi.org/10.1021/acsnano.5b05607.

[51] M. Moradi, M.H. Rahimian, S.F. Chini, Coalescence-induced droplet detachment on low-adhesion surfaces: A three-phase system study, Phys. Rev. E 99 (6) (2019) 1–13, http://dx.doi.org/10.1103/PhysRevE.99.063102.

[52] L. Xia, H. Yu, F. Chen, Z. Huo, D. Zhang, Y. Tian, Pillar height regulated droplet impact dynamics on pillared superhydrophobic surfaces, Int. J. Mech. Sci. 276 (2024) 109386, http://dx.doi.org/10.1016/J.IJMECSCI.2024.109386, URL https://linkinghub.elsevier.com/retrieve/pii/S0020740324004284.